

ORIGINAL RESEARCH OPEN ACCESS

Nested Horn-Based 3D-Printed Dual-Band High-Gain Conical Beam Antenna

Li Wu¹  | Sipei Wu¹ | Shuai Zhang² | Hui Xue¹ | Boyang Qian¹
¹School of Electronic and Optical Engineering, Nanjing University of Science and Technology, Nanjing, China | ²Shanghai Radio Equipment Research Institute, Shanghai, China

Correspondence: Li Wu (li_wu@njust.edu.cn)

Received: 23 October 2024 | **Revised:** 6 February 2025 | **Accepted:** 15 February 2025

Handling Editor: Ladislau Matekovits

Funding: The authors received no specific funding for this work.

Keywords: conical antennas | horn antennas | three-dimensional printing | ultra wideband antennas

ABSTRACT

Dual-band antennas have found extensive applications in the fields of communications, guidance, tracking systems, etc. However, traditional designs often struggle to simultaneously achieve high gain, wide impedance bandwidth and conical beam characteristics. In response to this challenge, a dual-band high-gain conical beam antenna with broad impedance bandwidth based on a nested horn operating at Ku-/Ka-band is presented in this paper. The nested horn excited by metal probes comprises a Ka-band circular waveguide horn and an outer nested Ku-band waveguide horn. The proposed antenna operates in the TM_{01} mode, demonstrating rotationally symmetrical field distribution, which enables the generation of conical beams. The utilisation of a ridge waveguide further widens the impedance bandwidth. The incorporation of dual reflectors enhances the directivity of electromagnetic wave propagation, leading to increased gain and a fixed beam pointing angle. The measured results show that the proposed antenna operates at 12.8–18 GHz in the Ku-band and 25.2–43.5 GHz in the Ka-band, with relative impedance bandwidths of approximately 33.8% and 53.3%, respectively, covering nearly the entire Ku-band and Ka-band. The peak gain reaches 12.2 dBi at 15 GHz and 16.4 dBi at 40 GHz. Furthermore, the maximum beam pointing angles are maintained at 30° for both frequency bands.

1 | Introduction

Conical beam (CB) antennas are characterised by their omnidirectional radiation patterns in the azimuth plane and the presence of nulls in the normal direction. These distinct radiation characteristics render CB antennas indispensable in a wide range of applications, including wireless local area networks (WLAN), target detection, tracking or guiding systems [1, 2]. Specifically, when observed from the ground, the elevation angles of satellites are always tilted from the boresight direction, making conical beam antennas suitable candidates for satellite

communication [3]. Meanwhile, the rapid advancements in millimetre-wave wireless communication technologies, driven by the demand for higher data rates, reduced latency and enhanced communication reliability, have driven the development of CB antennas featuring broad impedance bandwidth, dual-band operation and high gain.

Substantial efforts have been dedicated to the development of CB antennas, with circular patch antennas emerging as the most widely utilised solution for achieving the desired conical beam radiation patterns [4–6]. However, a notable limitation of these

This is an open access article under the terms of the [Creative Commons Attribution](https://creativecommons.org/licenses/by/4.0/) License, which permits use, distribution and reproduction in any medium, provided the original work is properly cited.

© 2025 The Author(s). *IET Microwaves, Antennas & Propagation* published by John Wiley & Sons Ltd on behalf of The Institution of Engineering and Technology.

antennas is their relatively low peak gain, which generally remains around 6 dBi. The employment of horns, open-ended waveguides and arrays has been shown to achieve relatively higher gains [2, 7, 8]. A conical beam array antenna with a nested horn as the concentric loop configuration using an element-level pattern diversity technique is presented in Ref. [2]. It realised 6% impedance bandwidth at a centre frequency of 10 GHz and a maximum gain of 11.9 dBi. Additionally, we proposed a wideband Ka-band circular aperture horn antenna with a conical radiation pattern realised by the metallic 3D printing technology [8]. A wide relative impedance bandwidth of 60.7% and a peak gain of 11.4 dBi can be achieved within the Ka-band. A slotted circular waveguide-based travelling-wave array antenna achieved a peak gain of 13.7 dBi, as demonstrated in Ref. [9]. Furthermore, reflectors are often utilised to increase the antenna gain [10–13]. A K-band conical beam-scanning reflector antenna with the reflector surface illuminated by two omnidirectional horns realised a maximum gain of 15 dBi at the pointing direction of 40° [11]. In Ref. [13], a CB antenna composed of a vertical monopole and circular side reflectors is reported to achieve a peak gain of 8.5 dBi. Nevertheless, a common limitation of these designs is that they operate in a single frequency band.

A variety of dual-band antennas have been investigated over the past decades, including dielectric resonator antennas (DRAs) [14–16], slotted-waveguide antenna arrays (SWAAs) [17], patches [18–21] and substrate integrated waveguides (SIWs) [22–24] et al. However, for these antennas operating at dual-band, the typical bandwidth is less than 15%, which is insufficient for high-data-rate communication systems. In Ref. [25], a dual-band high-gain CB antenna is proposed, consisting of a hollow dielectric resonator antenna (DRA) and a dielectric Fabry–Perot resonator antenna (FPRA). Although this design achieves wideband performance, it suffers from a relatively low gain of less than 3 dBi in the lower frequency band. In contrast, a dual-band cylindrical DRA presented in Ref. [26] demonstrates relative impedance bandwidths exceeding 14% and achieves peak gains of nearly 10 dBi in both frequency bands, offering a more balanced performance across the operational frequencies.

In pursuit of simultaneously achieving dual-band operation, CB radiation patterns and wide impedance bandwidth, several approaches have been explored [27, 28]. A nested dual-band horn CB antenna operating at the X-band and Ka-band is investigated in Ref. [29], whereas a slotted cylindrical waveguide antenna is proposed in Ref. [30]. However, designing a CB antenna that operates at dual frequencies with wide impedance bandwidth and high gain remains a significant challenge.

In this paper, a high-gain CB antenna operating in the Ku-band and Ka-band is presented. These two frequency bands are widely utilised in fixed wireless systems (14.4–15.35 GHz), fixed-satellite services (FSS) in the 14 and 17 GHz bands (14.5–14.8 GHz, 17.3–18.1 GHz), high-throughput satellites (HTS) in the 27.5–31 GHz range and high-altitude platform stations (HAPS) in the frequency ranges of 25.25–27.5 GHz, 27.9–28.2 GHz, 31–31.3 GHz and 38–39.5 GHz. The proposed antenna adopts a nested horn and reflector structure and operates in the TM₀₁ mode to ensure rotationally symmetrical field

distributions, which facilitates the generation of CB radiation. By employing a ridge waveguide and optimising its width, a smooth impedance transition from the waveguide to free space is achieved, effectively broadening the impedance bandwidth. Additionally, the directivity of the antenna is enhanced through the use of dual reflectors. To the best of our knowledge, this innovative design, which integrates a nested horn structure with dual reflectors, results in a dual-band high-gain CB antenna with broad impedance bandwidth that covers both the Ku-band and Ka-band, offering significant improvements over existing designs.

2 | Antenna Design and Analysis

The geometry of the proposed antenna is first introduced in this section. The principles behind broadband impedance bandwidth, conical beam formation and high gain are then discussed in detail. Furthermore, parametric studies are conducted to comprehensively analyse their effects on the antenna's performance.

2.1 | Antenna Geometry

The geometry of the proposed antenna is illustrated in Figure 1. It consists of a feed source, dual reflectors and connecting components. The dual reflectors comprise a main reflector and a subreflector. Moreover, the main reflector and the subreflector are connected and fixed by four brackets, whereas the feed source is positioned on a cylindrical support extending upwards from the main reflector.

As shown in Figure 2, the feed source adopts a dual-band nested horn antenna, which comprises an inner Ka-band antenna and an outer Ku-band antenna. The Ka-band antenna consists of a

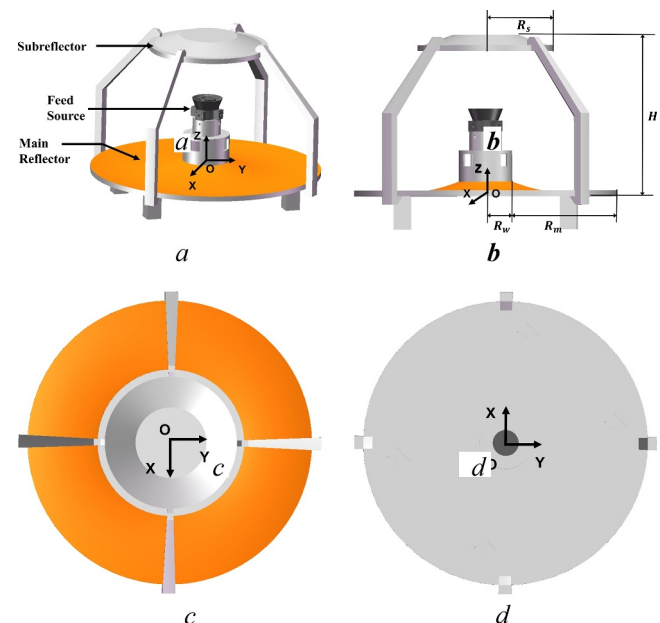


FIGURE 1 | Geometry of the proposed antenna: (a) isometric view, (b) side view, (c) top view and (d) bottom view.

coaxial waveguide and a quadruple-ridged conical horn. On the other hand, the Ku-band antenna adopts a coaxial waveguide horn structure with four sectorial ridges and is excited by four coaxial probes with equal amplitude and phase.

Detailed dimensions of the proposed feed horn are shown in Table 1.

The dual reflectors are bodies of revolution with a common symmetry axis, denoted as the Z-axis (see Figure 3). The subreflector is formed by revolving a segment of an elliptical curve around the symmetry axis. The subreflector features two foci, F_1 and F_2 , where Point F_1 lies on the symmetry Z-axis and defines the principal focus of the antenna, and Point A defines the vertex of the subreflector surface. The distance between the foci F_1 and F_2 is denoted as f . The distance from Point B on the edge of the subreflector to the Z-axis is the radius of the subreflector (named R_s , also shown in Figure 1b). The angle between $F_1 F_2$ and the Z-axis is recorded as α .

The main reflector is formed by revolving a parabola about the symmetry axis, with its geometry defined by Points D and C ,

corresponding to the inner and outer rims of the main reflector, respectively. To leave space for the feed access to the principal focus of the dual-reflector system, Point D is offset from the Z-axis. The focus of the main reflector is located at a point that coincides with one of the foci of the subreflector. The total radius of the main reflector is expressed as $R_m + R_w$ (also shown in Figure 1b). The angle between $F_2 E$ and the Z-axis is denoted as β . The equivalent phase centre of the feed source is placed at the antenna principal focus of Point F_1 , and the distance of $A F_1$ is denoted as p .

From the principles of geometric optics (GO), it is observed that a ray originating from the feed phase centre at Point F_1 reflects off both the subreflector and main reflector to reach the antenna aperture in a direction parallel to the parabola axis. This design transforms a spherical wavefront originating from Point F_1 into a conical wavefront at the antenna aperture. The shaping parameters of the dual reflector can be determined from the requirement for the antenna's beam pointing direction and gain [31]. Detailed dimensions of the shaping dual reflectors are shown in Table 2.

2.2 | Broadband Impedance Width Principle

As a crucial microwave transmission line, a ridge waveguide is formed by introducing one or more metal ridges into the cavity of rectangular or circular waveguides. Compared to standard

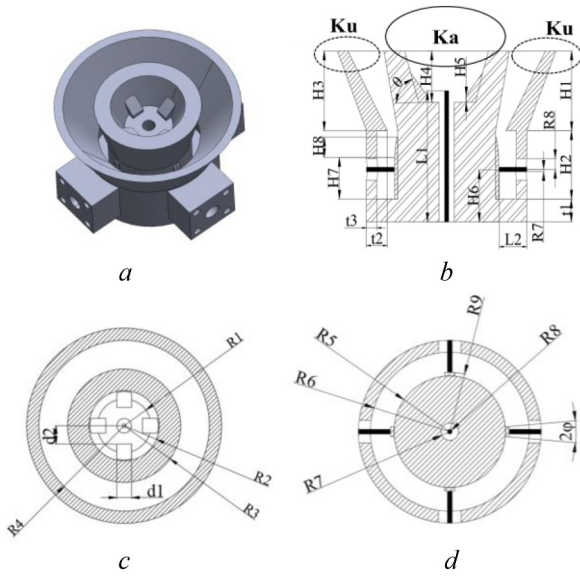


FIGURE 2 | Geometry of the feed horn: (a) isometric view, (b) cross-sectional view, (c) top view and (d) bottom view.

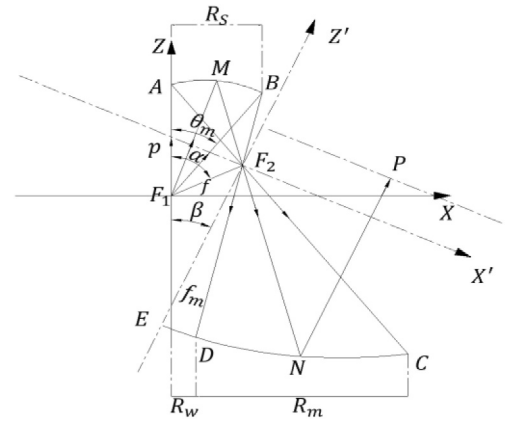


FIGURE 3 | Geometric parameters of the dual reflector.

TABLE 1 | Detailed dimensions of the proposed feed horn.

Parameter	Value	Parameter	Value	Parameter	Value
R_1	5.4 mm	H_1	14 mm	d_1	3.7 mm
R_2	8.05 mm	H_2	12 mm	d_2	3 mm
R_3	12.05 mm	H_3	14 mm	L_1	23 mm
R_4	25 mm	H_4	9 mm	L_2	5.13 mm
R_5	9.4 mm	H_5	1.1 mm	t_1	4 mm
R_6	13.4 mm	H_6	9.2 mm	t_2	4 mm
R_7	0.375 mm	H_7	7.3 mm	t_3	2 mm
R_8	1.46 mm	H_8	3.6 mm	θ	51.53°
R_9	10 mm			φ	5°

rectangular or circular waveguides, ridge waveguides offer several advantages, including lower characteristic impedance, reduced physical dimensions and broader bandwidth for single-mode transmission. By incorporating ridge waveguides into the aperture section of a horn antenna, the operational bandwidth can be significantly expanded [32–34].

The operating bandwidth of a reflector antenna is primarily determined by its feed source. To enhance the impedance bandwidth of the proposed antenna in the Ka-band, ridge structures are implemented at the aperture of the circular waveguide. Similarly, to broaden the impedance bandwidth in the Ku-band, four symmetrical ridges are integrated into the inner conductor of the coaxial waveguide. The presence of ridge edges induces edge capacitance effects, enabling widening of the bandwidth for circular waveguide horns operating in TM modes.

To realise better impedance matching, the impact of the ridges on the characteristic impedance of circular waveguides is analysed. The cross-sectional view of a ridged circular waveguide is shown in Figure 4.

A unit length of a ridged waveguide can be represented by a lumped-constant equivalent circuit consisting of capacitance and inductance in parallel. The capacitance C consists of the electrostatic capacitance C_0 , which is determined by the gap between the ridges, and the discontinuity capacitance C_d . Because the characteristics of the fundamental modes are primarily dependent on the ridge gap and thickness rather than the waveguide cross-section [35], the expression of total capacitance C derived for rectangular ridged waveguides [36] can also be applied to circular ridged waveguides:

$$C = C_0 + 2C_d = \frac{\epsilon s}{d} + 2C_d, \quad (1)$$

where ϵ represents the permittivity, and the discontinuity capacitance is approximately given by the following equation:

TABLE 2 | Geometric parameters of shaping dual reflectors.

Parameter	Value	Parameter	Value
p	68.1 mm	R_w	18 mm
f	60 mm	R_m	158 mm
f_m	91.4 mm	α	90°
R_s	70 mm	β	30°
H	194 mm		

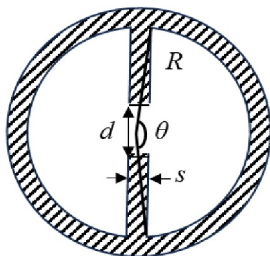


FIGURE 4 | Cross-sectional view of a ridged circular waveguide.

$$C_d = \frac{\epsilon}{\pi} \left[\frac{x^2 + 1}{x} \cos h^{-1} \left(\frac{1 + x^2}{1 - x^2} - 2 \ln \frac{4x}{1 - x^2} \right) \right], \quad (2)$$

where $x = d/b'$, $b' = 2\sqrt{R^2 - s^2}/4$.

The characteristic impedance of a unit length of a circular ridge waveguide can be expressed as follows:

$$Z_h = \frac{Z_{h,\infty}}{\sqrt{1 - \left(\frac{\lambda_0}{\lambda_c} \right)^2}}, \quad (3)$$

where $Z_{h,\infty}$ represents the characteristic impedance of the circular ridge waveguide as $\lambda_0 \rightarrow 0$, λ_c denotes the cutoff wavelength and λ_0 is the operating wavelength.

When $\lambda_0 \rightarrow 0$, the electromagnetic fields within the circular ridge waveguide can be considered to be concentrated between the ridges. The ridge waveguide can be treated as a strip transmission line with a characteristic impedance of

$$Z_{h,\infty} = \frac{V}{I} = \sqrt{\frac{L}{C}} = \frac{1}{v_\phi C} \quad (4)$$

where $v_\phi = \frac{1}{\sqrt{LC}} = \frac{1}{\sqrt{\mu\epsilon}}$, μ and ϵ denote the permeability and permittivity, respectively, then $Z_{h,\infty}$ can be further expressed as follows:

$$Z_{h,\infty} = \frac{1}{v_\phi C} = \frac{\sqrt{\mu\epsilon}}{C}. \quad (5)$$

Considering that $\sqrt{\frac{\mu}{\epsilon}}$ is the wave impedance, and it is approximately 377 Ω in free space, therefore, by combining Equation (1), $Z_{h,\infty}$ can be estimated as follows:

$$Z_{h,\infty} = \sqrt{\frac{\mu}{\epsilon}} \frac{\epsilon}{C} = \sqrt{\frac{\mu}{\epsilon}} \frac{\epsilon}{\frac{s}{d} + 2C_d} = \frac{377}{\frac{s}{d} + \frac{2C_d}{\epsilon}} \Omega. \quad (6)$$

Finally, the characteristic impedance of a unit length of the circular ridge waveguide can be given by the following equation:

$$Z_h = \frac{377}{\left(\frac{s}{d} + \frac{2C_d}{\epsilon} \right) \sqrt{1 - \left(\frac{\lambda_0}{\lambda_c} \right)^2}} \Omega. \quad (7)$$

To ensure effective impedance matching between the waveguide and free space, a gradual transition in the ridge geometry is typically implemented, which will facilitate a smooth impedance transformation. Furthermore, the gradual transition mitigates the risk of mode discontinuities induced by abrupt changes in the ridge profile, thereby maintaining stable wave propagation and minimising distortions in the waveguide. To achieve this gradual transition, an improved exponential function is employed in this study to describe the ridge contour, which is as follows:

$$y = Ae^{kx} + Cx. \quad (8)$$

The profile provides a mathematically continuous and smooth variation, ensuring optimal electromagnetic performance by reducing impedance mismatches while preserving the structural and fabrication integrity of the waveguide design.

As illustrated in Figure 5, the coefficients of the ridge contour function can be derived from the ridge spacing b , the length of the flared section of the circular horn L and the aperture diameter of the horn D_y . These parameters collectively define the geometric and functional characteristics of the ridge profile, ensuring optimal performance in impedance matching.

2.3 | Conical Beam Principle

The principle of achieving CB radiation can be illustrated from the perspective of field distributions of the feed source. The field distributions of the feed source at 15 and 35 GHz are depicted in Figure 6. At 15 GHz, the electromagnetic field distributions within a cross-section located 10 mm inward from the proposed antenna aperture are shown in Figures 6a,b. Through the excitation of four coaxial probes with equal amplitude and

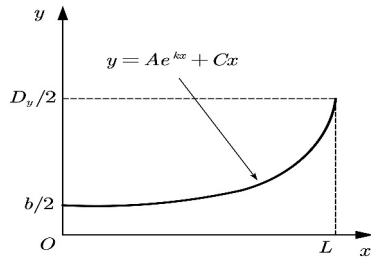


FIGURE 5 | Schematic representation of the ridge contour.

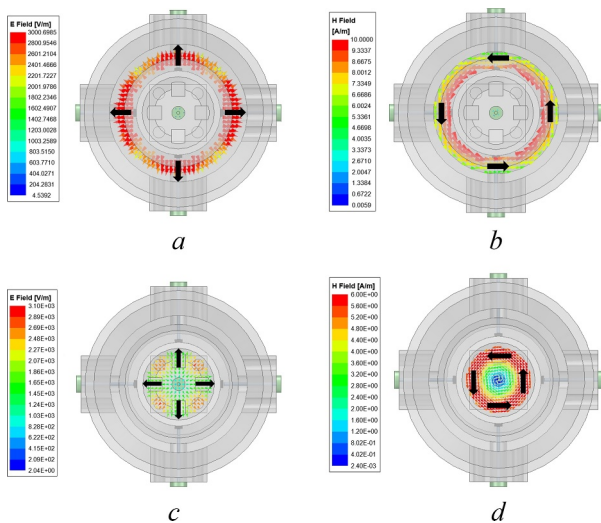


FIGURE 6 | Field distributions of dual-band feed: (a) electric field distribution at 15 GHz, (b) magnetic field distribution at 15 GHz, (c) electric field distribution at 35 GHz and (d) magnetic field distribution at 35 GHz.

phase, the electric field exhibits a radially symmetrical distribution, whereas the magnetic field distribution forms a closed loop around the circumference. This configuration successfully excites the TM_{01} mode, resulting in the desired conical beam (CB) radiation pattern. When the Ka-band antenna operates at 35 GHz, the electromagnetic field distribution within a cross-section situated 3 mm inward from the antenna aperture is shown in Figures 6c,d. In this case, the internal electric field is distributed symmetrically along the radial direction, and the magnetic field distribution remains a closed loop around the circumference. This configuration also successfully excites the TM_{01} mode, leading to the radiation of an omnidirectional CB.

The radiation patterns of the feed horn at 13 GHz, 15 GHz and 17 GHz are presented in Figure 7. The antenna exhibits gains of 8.4 dBi, 10.2 dBi and 10.3 dBi with corresponding sidelobe levels of -14.2 dB, -14.1 dB and -10.2 dB at the respective frequencies.

Similarly, the radiation patterns of the proposed feed antenna are illustrated in Figure 8 for frequencies of 27 GHz, 35 GHz and 40 GHz. The proposed antenna achieves gains of 7.1 dBi, 9.5 dBi and 11.8 dBi with sidelobe levels of -14.9 dB, -19.5 dB and -17.5 dB at these frequency points.

2.4 | High-Gain Principle

Based on the principle of geometric optics, the spherical wave emanating from the feed source traverses through the focus F_1 towards the subreflector by adjusting the appropriate parameters. Then, it undergoes reflection off the subreflector, ultimately arriving at the main reflector through the other focus F_2 . Drawing upon the geometric principles of the ellipse and the parabola, the electromagnetic waves emitted by the feed source reach the aperture of the main reflector with the same phase difference. Therefore, the electromagnetic wave at the aperture

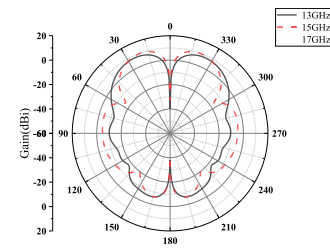


FIGURE 7 | Radiation patterns of the feed horn at 13, 15 and 17 GHz with gains of 8.4, 10.2 and 10.3 dBi, respectively.

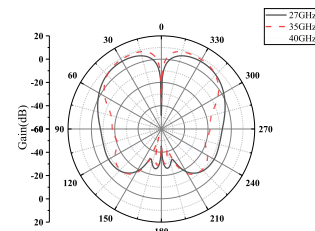


FIGURE 8 | Radiation patterns of the feed horn at 27, 35 and 40 GHz with gains of 7.1, 9.5 and 11.8 dBi, respectively.

surface exhibits uniform amplitude and phase, which is beneficial for enhancing the gain.

As shown in Figure 9, the simulated radiation patterns of the nested horn antenna with and without the dual reflectors are compared in the elevation plane ($\phi = 0^\circ$ corresponding to the cut plane at XOZ). It is observed that the maximum radiation direction of the conical beams at 15 and 35 GHz occurs at 30° with reflectors. At 15 GHz, the gain is increased by 2.2 dBi, 2.1 dBi and 2.2 dBi with the introduction of the reflectors in the elevation planes of $\phi = 0^\circ$, $\phi = 45^\circ$ and $\phi = 90^\circ$, respectively. At 35 GHz, the gain improves significantly with the reflectors, increasing from 9.5 dBi, 9.5 dBi and 9.4 dBi to 16.1 dBi, 16.3 dBi and 16.2 dBi in the respective elevation planes.

2.5 | Parametric Studies

Several key parameters of the proposed feed horn are critical in achieving a wide impedance bandwidth. To thoroughly analyse their impact on performance, parametric studies were conducted. This study specifically investigates the effects of varying the angle of the sectorial ridges (φ), the radius of the ridges (R_9), the ridge width (d_l) and vertical height (H_5) on the impedance bandwidth within the Ku-band and the Ka-band, respectively. The influences of these parameters are examined in detail to provide a comprehensive understanding of their roles in optimising the feed horn's impedance bandwidth.

From Figures 10a,b, it can be observed that both the angle φ and the radius R_9 of the sectorial ridges significantly influence the impedance bandwidth in the Ku-band. An increase in φ leads to deteriorated antenna matching, thereby narrowing the

impedance bandwidth. Conversely, as R_9 increases, the distance between the probes and the sectorial ridges decreases, resulting in increased equivalent capacitance, which has a pronounced effect on the characteristic impedance in the Ku-band.

From Figure 10c, it is evident that increasing H_5 generally enhances antenna matching. Specifically, as H_5 increases from 1.0 to 1.1 mm, the impedance bandwidth expands. However, further increasing H_5 to 1.2 mm results in a reduction of the bandwidth. In contrast, as the ridge width d_l increases, the antenna's impedance matching gradually deteriorates. Notably,

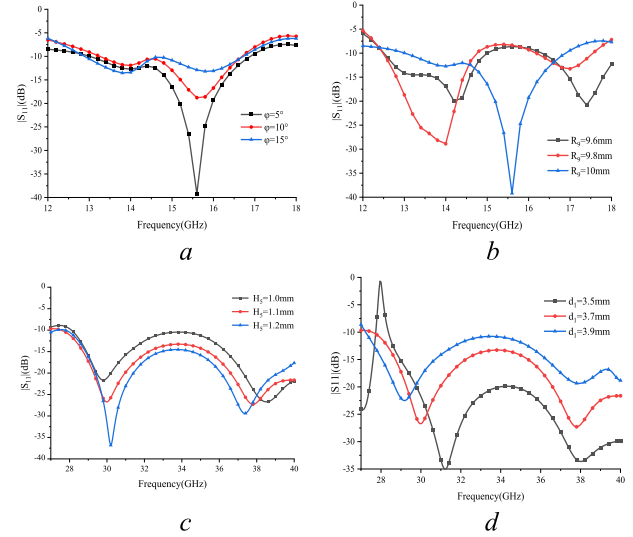


FIGURE 10 | Effects of ridge parameters on feed reflection coefficients: (a) $\varphi = 5^\circ, 10^\circ, 15^\circ$, (b) $R_9 = 9.6, 9.8, 10$ mm, (c) $H_5 = 1.0, 1.1, 1.2$ mm and (d) $d_l = 3.5, 3.7, 3.9$ mm.

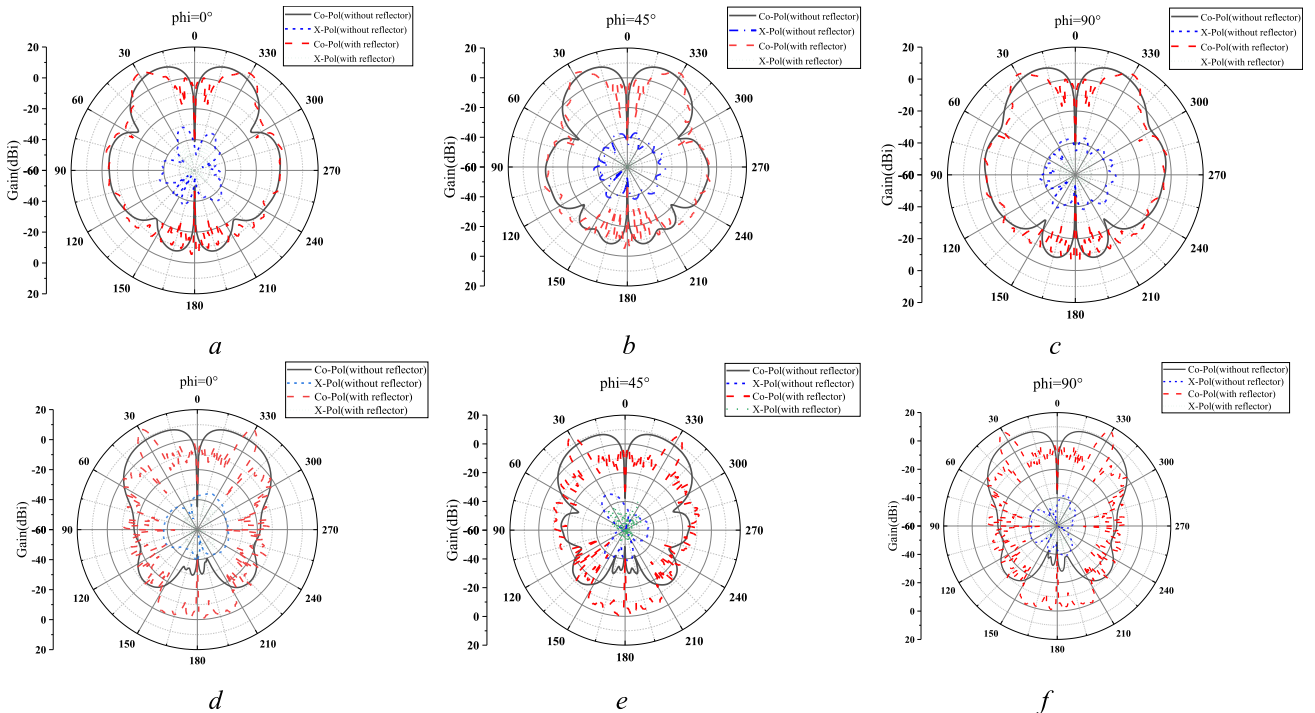


FIGURE 9 | Comparison of radiation patterns with and without reflectors in the elevation plane: 15 GHz at (a) $\phi = 0^\circ$, (b) $\phi = 45^\circ$, (c) $\phi = 90^\circ$ and 35 GHz at (d) $\phi = 0^\circ$, (e) $\phi = 45^\circ$, (f) $\phi = 90^\circ$.

when $d_t = 3.5$ mm, an impedance mismatch occurs around 28.2 GHz, leading to a narrower impedance bandwidth.

Furthermore, the effects of these parameters on the antenna's far-field radiation pattern were evaluated through simulations. The results indicate that the ridge parameters have an insignificant effect on the radiation patterns.

3 | Antenna Measurement and Discussions

The proposed antenna was simulated and optimised with the full-wave simulation software FEKO. To verify the performance of the proposed antenna, an antenna prototype was fabricated and experimentally measured. Considering the complex structure, the feed source was fabricated by an iSLM28 3D printer using direct metal laser sintering (DMLS) by laser sintering the AISi10Mg powder layer by layer. The dual reflectors were fabricated utilising a stereoscopic light apparatus (SLA) for 3D printing with photosensitive resin. Postprinting, the surfaces underwent meticulous polishing and cleaning procedures to achieve high-quality surface smoothness conducive to subsequent metallisation processes. Lastly, the surfaces of the reflectors were metallised with copper. A power divider (Model: QY-PS4-2/18-SE) from Qi Yuan Microwave Technology is utilised as the feeding network to excite the Ku-band antenna. The power divider operates over a frequency range of 2–18 GHz, with a maximum input and output port VSWR of less than 1.5. The photograph of the 3D-printed antenna is shown in Figure 11.

The reflection coefficients of the fabricated antenna were measured using a vector network analyser N5244 A, as shown in Figure 12. In the Ku-band, the simulated -10 dB relative impedance bandwidth is 27.4% (12.9–17 GHz), whereas the measured -10 dB impedance bandwidth is 33.8% (12.8–18 GHz). In the Ka-band, the measured bandwidth of the proposed antenna spans from 25.2 to 43.5 GHz, which corresponds to a -10 dB impedance bandwidth of 53.3%.

The simulated and measured radiation patterns of the proposed antenna in the XOZ plane at 13 GHz, 15 GHz and 17 GHz for Ku-band and at 27 GHz, 35 GHz and 40 GHz for Ka-band are presented in Figure 13. The measured gains of the proposed antenna are 11.8 dBi, 12.2 dBi and 11 dBi at 13 GHz, 15 GHz and 17 GHz, respectively, showing deviations of 1.3 dB, 0.2 dB and 0.4 dB from the simulated values. The corresponding measured sidelobe levels are -10.3 dB, -10.4 dB and -11.3 dB. In the Ka-band, the measured gains are 13.2 dBi, 15.7 dBi and 16.4 dBi at 27 GHz, 35 GHz and 40 GHz, respectively, which are 0.2 dB, 0.4 dB and 0.5 dB lower than the simulated values. The measured sidelobe levels are -8.5 dB, -15.2 dB and -13.8 dB. Furthermore, the measured maximum pointing angles show close agreement with the simulation results, confirming the antenna's stable directional behaviour across the operating frequencies.

Additionally, the simulated and measured radiation patterns of the proposed antenna at 15 and 35 GHz in the elevation planes of $\phi = 45^\circ$ and 90° are presented in Figure 14. It can be



FIGURE 11 | Picture of the proposed antenna.

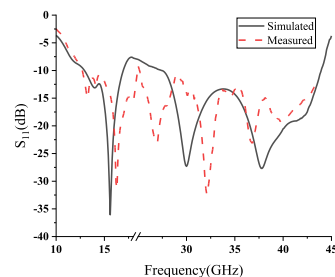


FIGURE 12 | Comparison of measured and simulated reflection coefficients for the proposed antenna.

observed that gains vary within a small range of 0.5 dB at 15 GHz (12.2 dBi@ $\phi = 0^\circ$, 11.7 dBi@ $\phi = 45^\circ$, 11.8 dBi@ $\phi = 90^\circ$). The sidelobe levels in the elevation planes of $\phi = 45^\circ$ and 90° are -10.4 dB and -8.3 dB, respectively. Similarly, at 35 GHz, the gains are 15.9 dBi and 15.4 dBi in the elevation planes of $\phi = 45^\circ$ and 90° , demonstrating good gain stability. The sidelobe levels at this frequency are -10.2 dB and -15.1 dB in the respective elevation planes.

From the measured gain results within the two operating bands as illustrated in Figure 15, it can be observed that the gain ranges from 11 dBi to 12.2 dBi within the frequency range of 13–17 GHz and from 13.2 dBi to 16.4 dBi within the frequency range of 27–40 GHz, demonstrating the stable performance of the proposed antenna. It is important to note that the measured gains in the Ku-band do not include the insertion loss of the power divider feeding network.

As shown in Figure 16, the measured radiation efficiency ranges from 82.8% to 95.7% within the frequency range of 13–17 GHz. For the frequency range of 27–40 GHz, the measured radiation efficiency varies from 81.3% to 95.9%. These results indicate that the antenna maintains good radiation efficiency across its entire operating frequency range.

A detailed comparison of the proposed antenna with other reported designs is summarised in Table 3, considering operating frequency, antenna type, impedance bandwidth, peak gain, pointing direction, sidelobe level, radiation efficiency and maximum dimension.

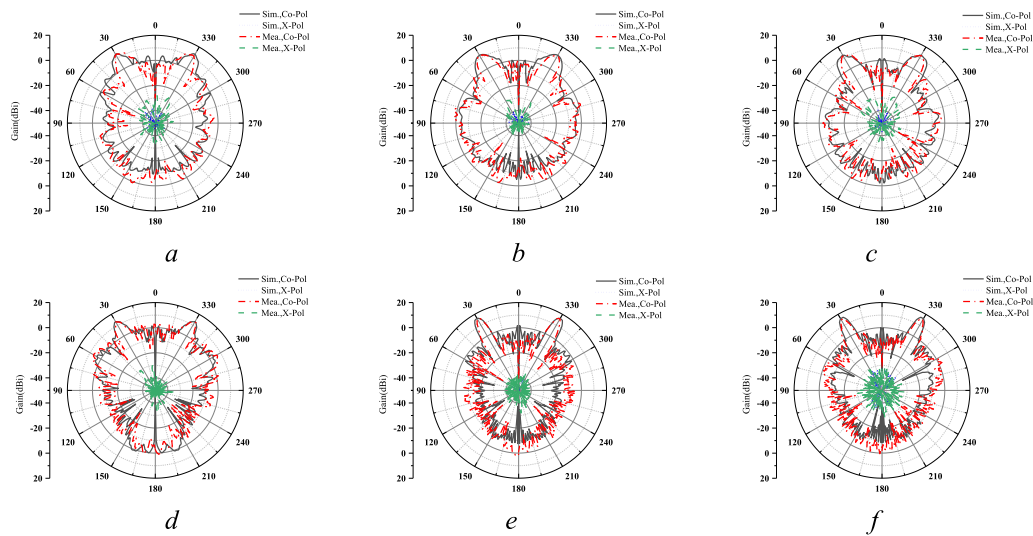


FIGURE 13 | Simulated and measured radiation patterns at different frequencies of the proposed antenna: (a) 13 GHz, (b) 15 GHz, (c) 17 GHz, (d) 27 GHz, (e) 35 GHz and (f) 40 GHz.

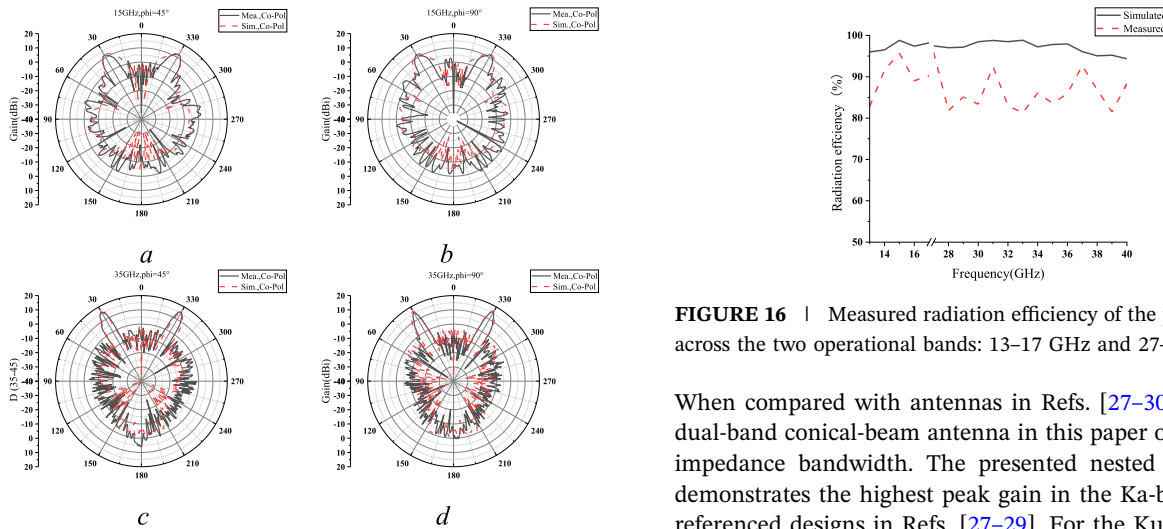


FIGURE 14 | Measured radiation patterns of the proposed antenna: 15 GHz at (a) $\phi = 45^\circ$, (b) $\phi = 90^\circ$ and 35 GHz at (c) $\phi = 45^\circ$, (d) $\phi = 90^\circ$.

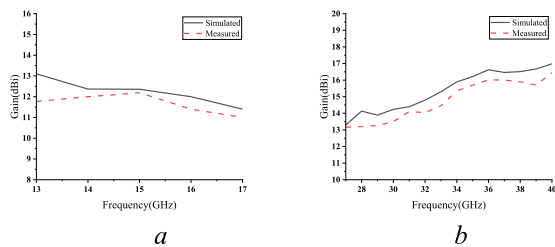


FIGURE 15 | Simulated and measured gain results within the two operational bands: (a) 13–17 GHz and (b) 27–40 GHz.

Compared to the single-band conical-beam antennas with high gain reported in Refs. [2, 10, 13], the proposed antenna not only operates in dual frequency bands but also demonstrates wider impedance bandwidths and higher gains. Although the antennas with reflectors in Refs. [11, 12] achieve comparable gains, they are limited by narrow impedance bandwidths.

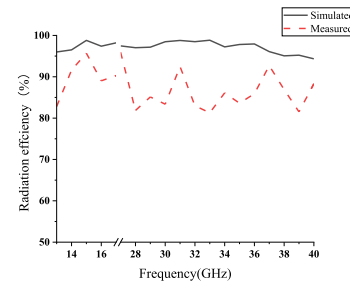


FIGURE 16 | Measured radiation efficiency of the proposed antenna across the two operational bands: 13–17 GHz and 27–40 GHz.

When compared with antennas in Refs. [27–30], the proposed dual-band conical-beam antenna in this paper offers the largest impedance bandwidth. The presented nested feed horn also demonstrates the highest peak gain in the Ka-band among the referenced designs in Refs. [27–29]. For the Ku-band, the peak gain of the proposed nested horn is similar to the low-frequency band gains reported in Refs. [28, 29] when accounting for a feeding network insertion loss of approximately 1.5 dB. The peak gain is further increased by 1.8 and 5.1 dB for the Ku-band and Ka-band, respectively, after introducing the reflector. The proposed dual-band conical beam antenna achieves both wide impedance bandwidths and high gains across both frequency bands, offering a clear advantage over existing designs.

Additionally, except for the antenna in Ref. [11], which achieves beam scanning through mechanical adjustment of the feed position, all other antennas have a fixed pointing direction. The measured worst sidelobe levels of the proposed antenna among the different elevation planes are -8.3 dB at 15 GHz and -10.2 dB at 35 GHz. Furthermore, the radiation efficiencies of the proposed dual-band conical beam antenna are comparable to those reported in Refs. [12, 13, 30]. Regarding the antenna volume, the proposed nested feed horn exhibits a dimensional size comparable to the designs referenced in Refs. [28, 29]. However, the introduction of the reflector results in a larger overall volume for all reflector-based designs compared to the other antennas.

TABLE 3 | Performance for the proposed and reference antennas.

Ref.	Frequency (GHz)	Technique	Impedance bandwidth (%)	Peak gain (dBi)	Pointing direction	Sidelobe level (dB)	Radiation efficiency (%)	Volume
[2]	10(Single)	Horn array	6	11.9	18°	~-15 ^a	N.A.	$\phi 3.9\lambda_1 \times 1.5\lambda_1$
[10]	35(Single)	Horn with reflector	1.1	12	50°	-11	N.A.	$\phi 31.5\lambda_1 \times 7\lambda_1$
[11]	24(Single)	Horn with reflector	11	15	30.8°–45.2°	~-14 ^a	50	$\phi 36\lambda_1 \times N.A$
[12]	34(Single)	Patch with reflector	13	16.6	16°	-18.1	83.3	$\phi 45.8\lambda_1 \times 21.1\lambda_1$
[13]	28.3(Single)	Monopole with side reflector	11.6	8.5	22°	~-4 ^a	88.3	$\phi 4.5\lambda_1 \times 0.5\lambda_1$
[27]	14/35 (Dual)	Monopole	20.8/10.1	5.4/9.9	40°/25° ^a	-11.8/-15.2	N.A.	$\phi 1.4\lambda_1 \times 0.05\lambda_1 / \phi 3.5\lambda_2 \times 0.17\lambda_2$
[28]	25/34 (Dual)	Nested horn	4.4/6.2	8.8/6.4	23°/38°	~ -18/-10 ^a	N.A.	$2.78\lambda_1 \times 2.45\lambda_1 \times 3.03\lambda_1 / 3.78\lambda_1 \times 3.33\lambda_1 \times 4.12\lambda_1$
[29]	10/35 (Dual)	Nested horn	12.5/8.5	8.8/11.2	21°/21°	~ -14/-16 ^a	N.A.	$\phi 1.94\lambda_1 \times 1.69\lambda_1 / \phi 6.8\lambda_2 \times 5.9\lambda_2$ ^a
[30]	28/38.5 (Dual)	Waveguide array antenna	14.3/7.8	14.5/14.2	29°/38°	~-7/-6 ^a	83/93	$\phi 0.7\lambda_1 \times 24.5\lambda_1 / \phi 0.96\lambda_2 \times 33.7\lambda_2$
This study	15/35 (Dual)	Nested horn with reflector	33.8/53.3	10.4/11.3#1 12.2/ 16.4#2	30°/30°#2	-8.3/ -10.2#2	95.7/83.6#2	$\phi 2.5\lambda_1 \times 1.5\lambda_1 / \phi 5.8\lambda_2 \times 3.5\lambda_2$ ^{#1} $\phi 17.6\lambda_1 \times 9.7\lambda_1 / \phi 41.1\lambda_2 \times 22.7\lambda_2$ ^{#2}

Note: #1 nested horn. #2 with reflector. λ_1 is the free-space wavelength for the low-frequency band, and λ_2 is the free-space wavelength for the high-frequency band.

^aNot provided. Estimated.

4 | Conclusion

In this paper, a 3D-printed dual-band high-gain conical beam antenna based on a nested horn is presented. The nested horn, consisting of the Ka-band circular waveguide horn and the outer Ku-band waveguide horn, is employed to realise the dual-band property. The proposed antenna operates in the TM_{01} mode, which generates a rotationally symmetrical field distribution, resulting in CB radiation. The design incorporates a ridge waveguide to ensure a smooth transition from the waveguide to free space, thus achieving wider impedance bandwidths. Additionally, the dual reflectors enhance the directionality of electromagnetic wave propagation. The measured results confirm that the proposed antenna exhibits distinct dual-band characteristics. In the Ku-band, the antenna operates over a frequency range of 12.8–18 GHz, with a relative impedance bandwidth of 33.8%. In the Ka-band, it operates from 25.2 to 43.5 GHz, offering a relative impedance bandwidth of 53.3%.

Author Contributions

Li Wu: conceptualisation, formal analysis, writing – original draft, writing – review and editing. **Sipei Wu:** investigation, writing – original draft. **Shuai Zhang:** conceptualisation, validation. **Hui Xue:** methodology. **Boyang Qian:** validation, visualization.

Conflicts of Interest

The authors declare no conflicts of interest.

Data Availability Statement

The data that support the findings of this study are available from the corresponding author upon reasonable request.

References

1. N. J. McEwan, R. A. Abd-Alhameed, E. M. Ibrahim, P. S. Excell, and J. G. Gardiner, “A New Design of Horizontally Polarized and Dual-Polarized Uniplanar Conical Beam Antennas for HIPERLAN,” *IEEE Transactions on Antennas and Propagation* 51, no. 2 (2003): 229–237, <https://doi.org/10.1109/tap.2003.809058>.
2. D. Hua, S. S. Qi, W. Wu, and D. G. Fang, “Synthesis of Conical Beam Array Antenna With Concentric Loop Configuration Using Element-Level Pattern Diversity Technique,” *IEEE Transactions on Antennas and Propagation* 66, no. 11 (2018): 6397–6402, <https://doi.org/10.1109/tap.2018.2867041>.
3. X. Bai, X. Liang, M. Li, B. Zhou, J. Geng, and R. Jin, “Dual-Circularly Polarized Conical-Beam Microstrip Antenna,” *IEEE Antennas and Wireless Propagation Letters* 14 (2014): 482–485, <https://doi.org/10.1109/lawp.2014.2369515>.
4. A. Al-Zoubi, F. Yang, and A. Kishk, “A Broadband Center-Fed Circular Patch-Ring Antenna With a Monopole Like Radiation Pattern,” *IEEE Transactions on Antennas and Propagation* 57, no. 3 (2009): 789–792, <https://doi.org/10.1109/tap.2008.2011406>.

5. J. Liu, Q. Xue, H. Wong, H. W. Lai, and Y. Long, "Design and Analysis of a Low-Profile and Broadband Microstrip Monopolar Patch Antenna," *IEEE Transactions on Antennas and Propagation* 61, no. 1 (2013): 11–18, <https://doi.org/10.1109/tap.2012.2214996>.
6. J. Liu, S. Zheng, Y. Li, and Y. Long, "Broadband Monopolar Microstrip Patch Antenna With Shorting Vias and Coupled Ring," *IEEE Antennas and Wireless Propagation Letters* 13 (2014): 39–42.
7. H. S. Lin, Y. J. Cheng, and Y. Fan, "Synthesis of Difference Patterns for 3-D Conformal Beam-Scanning Arrays With Asymmetric Radiation Aperture," *IEEE Transactions on Antennas and Propagation* 70, no. 9 (2022): 8040–8050, <https://doi.org/10.1109/tap.2022.3164232>.
8. L. Wu, C. Wang, S. S. Peng, and Y. Y. Guo, "3-D Printed Wideband Millimeter-Wave Horn Antenna With Conical Radiation Pattern," *IEEE Antennas and Wireless Propagation Letters* 19, no. 3 (2020): 453–456, <https://doi.org/10.1109/lawp.2019.2963747>.
9. P. Sanchez-Olivares, J. L. Masa-Campos, E. Garcia-Marin, and D. Escalona-Moreno, "High-Gain Conical-Beam Traveling-Wave Array Antenna Based on a Slotted Circular Waveguide at Ku-Band," *IEEE Transactions on Antennas and Propagation* 68, no. 8 (2020): 6435–6440, <https://doi.org/10.1109/tap.2020.2970031>.
10. S. S. Qi, W. Wu, and D. G. Fang, "High Gain Conical Beam Antenna With Large Beam-Pointing Angle by Using Hemitorus Lens-Reflector," *Proc. AsiaPacific Conf. Antennas Propag. Harbin, China, July* (2014): 430–432, <https://doi.org/10.1109/apcap.2014.6992517>.
11. J. Yang, S.-S. Qi, W. Wu, and D.-G. Fang, "A Novel High-Gain Sum and Difference Conical Beam-Scanning Reflector Antenna," *IEEE Access* 8 (2020): 103291–103300, <https://doi.org/10.1109/access.2020.2998835>.
12. Y. Yu, B. Qian, Y. Gao, Y. Wang, and L. Wu, "A Ka-Band Antenna With High-Gain and Conical Beam," in *2022 Asia-Pacific Microwave Conference (APMC)*, (Yokohama, Japan, December 2022), 845–847.
13. D. A. Pham, M. Lee, and S. Lim, "High-gain Conical-Beam Planar Antenna for Millimeter-Wave Drone Applications," *IEEE Transactions on Antennas and Propagation* 69, no. 10 (2021): 6959–6964, <https://doi.org/10.1109/tap.2021.3070662>.
14. H. M. Chen, Y. K. Wang, Y. F. Lin, S. C. Lin, and S. C. Pan, "A Compact Dual-Band Dielectric Resonator Antenna Using a Parasitic Slot," *IEEE Antennas and Wireless Propagation Letters* 8 (2009): 173–176.
15. Y. Ding and K. W. Leung, "On the Dual-Band DRA-Slot Hybrid Antenna," *IEEE Transactions on Antennas and Propagation* 57, no. 3 (2009): 624–630, <https://doi.org/10.1109/tap.2009.2013433>.
16. L. X. Cui, X. H. Ding, W. W. Yang, L. Guo, L. H. Zhou, and J. X. Chen, "Communication Compact Dual-Band Hybrid Dielectric Resonator Antenna for 5G Millimeter-Wave Applications," *IEEE Transactions on Antennas and Propagation* 71, no. 1 (2023): 1005–1010, <https://doi.org/10.1109/tap.2022.3211389>.
17. E. C. Vilas Boas, H. R. D. Filgueiras, I. Feliciano da Costa, J. A. J. Ribeiro, and A. C. Sodre, "Dual-Band Switched-Beam Antenna Array for MIMO Systems," *IET Microwaves, Antennas & Propagation* 14, no. 1 (2020): 82–87, <https://doi.org/10.1049/iet-map.2019.0010>.
18. D. W. Huang and Z. W. Du, "Wideband Dual-Band Dual-Polarised Antenna With Less Layer Radiating Patch," *IET Microwaves, Antennas & Propagation* 13, no. 8 (2019): 1214–1218, <https://doi.org/10.1049/iet-map.2018.5688>.
19. P. L. Vijayvergiya and R. K. Panigrahi, "Single-Layer Single-Patch Dual Band Antenna for Satellite Applications," *IET Microwaves, Antennas & Propagation* 11, no. 5 (2017): 664–669, <https://doi.org/10.1049/iet-map.2016.0393>.
20. W.-W. Chen, Q.-S. Wu, and X. Zhang, "Quad-mode Dual-Band Dual-Sense Circularly Polarized Microstrip Patch Antenna," *IEEE Antennas and Wireless Propagation Letters* 23, no. 5 (2024): 1503–1507, <https://doi.org/10.1109/lawp.2024.3360271>.
21. M. Wei, J. Wang, X. Wang, T. Liu, Y. Lu, and Y. Gao, "Low-Profile Dual-Band Microstrip Patch Antenna With Shorting Pins," *IEEE Antennas and Wireless Propagation Letters* 23, no. 6 (2024): 1834–1838, <https://doi.org/10.1109/lawp.2024.3370724>.
22. M. P. Shen, X. Geng, X. Yang, W.-W. Yang, and J.-X. Chen, "An Extremely Small-Footprint Dual-Wideband Stacked Antenna Based on Quarter-Mode Substrate Integrated Waveguide," *IEEE Antennas and Wireless Propagation Letters* 23, no. 10 (2024): 2994–2998, <https://doi.org/10.1109/lawp.2024.3417468>.
23. Y. X. Sun, D. Wu, X. S. Fang, and N. Yang, "Compact Quarter-Mode Substrate-Integrated Waveguide Dual-Frequency Millimeter-Wave Antenna Array for 5G Applications," *IEEE Antennas and Wireless Propagation Letters* 19, no. 8 (2020): 1405–1409, <https://doi.org/10.1109/lawp.2020.3003305>.
24. C.-M. Liu, S. Q. Xiao, and K. Wu, "Miniaturized Cylindrical Open-Ended SIW Cavity Antenna and its Dual-Band Applications," *IEEE Transactions on Antennas and Propagation* 69, no. 8 (2021): 4390–4400, <https://doi.org/10.1109/tap.2020.3048553>.
25. T. Yang, Z. Wang, Y. Cao, J. Ren, and Y. Yin, "Wideband Dual-Port Dual-Band Antenna With Large Frequency Ratio," in *2022 IEEE Conference on Antenna Measurements and Applications (CAMA)* (Guangzhou, China, December 2022), 1–3.
26. T. Li and Z. N. Chen, "A Dual-Band Metasurface Antenna Using Characteristic Mode Analysis," *IEEE Transactions on Antennas and Propagation* 66, no. 10 (2018): 5620–5624, <https://doi.org/10.1109/tap.2018.2860121>.
27. C. C. Shan, S. Zhang, H. Xue, L. Wu, and Y. J. Rong, "A Dual-Band Broadband Conical Beam Antenna Based on TM₀₁ and TM₀₂ Mode," in *2023 Asia-Pacific Microwave Conference (APMC)* (Taipei, Taiwan, December 2023), 512–514.
28. J. X. Li, S. F. Wu, Y. J. Li, X. M. Chen, S. Yan, and X.-Y. Zhang, "SLA Printed Dual-Band Conical-Beam Filtering Antenna," *IEEE Antennas and Wireless Propagation Letters* 22, no. 10 (2023): 2462–2466, <https://doi.org/10.1109/lawp.2023.3291386>.
29. S. S. Qi, W. Wu, and D. G. Fang, "Dual/Single Band Conical-Beam Nested Horn Antennas With Dual/single Pointing Angles," *IEEE Transactions on Antennas and Propagation* 60, no. 10 (2012): 4911–4915, <https://doi.org/10.1109/tap.2012.2207342>.
30. P. Sanchez-Olivares, J. L. Masa-Campos, and E. Garcia-Marin, "Dual-polarization and Dual-Band Conical-Beam Array Antenna Based on Dual-Mode Cross-Slotted Cylindrical Waveguide," *IEEE Access* 9 (2021): 94109–94121, <https://doi.org/10.1109/access.2021.3093204>.
31. F. J. da Silva Moreira and J. R. Bergmann, "Axis-Displaced Dual-Reflector Antennas for Omnidirectional Coverage With Arbitrary Main-Beam Direction in the Elevation Plane," *IEEE Transactions on Antennas and Propagation* 54, no. 10 (2006): 2854–2861, <https://doi.org/10.1109/tap.2006.882181>.
32. C. Bruns, P. Leuchtmann, and R. Vahldieck, "Analysis and Simulation of a 1-18-GHz Broadband Double-Ridged Horn Antenna," *IEEE Transactions on Electromagnetic Compatibility* 45, no. 1 (2003): 55–60.
33. Z. Y. Li, X. R. Ba, Z. P. Wang, X. M. Chen, and S. Gao, "A Wideband Dual-Circularly Polarized Inverted Quad-Ridged Elliptical Waveguide Horn Antenna," *IEEE Antennas and Wireless Propagation Letters* 23, no. 10 (2024): 2850–2854, <https://doi.org/10.1109/lawp.2024.3409419>.
34. Y. Cao, G. A. E. Vandenbosch, and S. Yan, "Low-Profile Dual-Polarized Multi-Beam Antenna Based on Pillbox Reflector and 3D-Printed Ridged Waveguide," *IEEE Transactions on Antennas and Propagation* 70, no. 9 (2022): 7578–7591, <https://doi.org/10.1109/tap.2022.3171728>.
35. W. Sun and C. A. Balanis, "Analysis and Design of Quadruple-Ridged Waveguides," *IEEE Transactions on Microwave Theory and*

Techniques 42, no. 12 (1994): 2201–2207, <https://doi.org/10.1109/22.339743>.

36. T. S. Chen, “Calculation of the Parameters of Ridge Waveguides,” *IRE Trans. Microw. Theory Tech* 5, no. 1 (1957): 12–17, <https://doi.org/10.1109/tmtt.1957.1125084>.